Systems/Circuits

The Firing of Theta State-Related Septal Cholinergic Neurons Disrupt Hippocampal Ripple Oscillations via Muscarinic Receptors

Xiaoyu Ma,[1*] Yiyao Zhang,[1*] Lina Wang,[1] Na Li,[1] Edi Barkai,[4] Xiaohui Zhang,[5] Longnian Lin,[1,2,3] and Jiamin Xu[1]

[1]Shanghai Key Laboratory of Brain Functional Genomics (Ministry of Education), School of Life Science, East China Normal University, Shanghai, 200062, China, [2]NYU–ECNU Institute of Brain and Cognitive Science, New York University Shanghai, Shanghai, 200062, China, [3]Tongji University Brain and Spinal Cord Clinical Center, Shanghai, 200062, China, [4]Sagol Department of Neurobiology, Faculty of Natural Sciences, University of Haifa, Haifa, 3498838 Israel, and [5]State Key Laboratory of Cognitive Neuroscience & Learning, Beijing Normal University, Beijing, 100875, China

The septo-hippocampal cholinergic system is critical for hippocampal learning and memory. However, a quantitative description of the *in vivo* firing patterns and physiological function of medial septal (MS) cholinergic neurons is still missing. In this study, we combined optogenetics with multichannel *in vivo* recording and recorded MS cholinergic neuron firings in freely behaving male mice for 5.5–72 h. We found that their firing activities were highly correlated with hippocampal theta states. MS cholinergic neurons were highly active during theta-dominant epochs, such as active exploration and rapid eye movement sleep, but almost silent during non-theta epochs, such as slow-wave sleep (SWS). Interestingly, optogenetic activation of these MS cholinergic neurons during SWS suppressed CA1 ripple oscillations. This suppression could be rescued by muscarinic M_2 or M_4 receptor antagonists. These results suggest the following important physiological function of MS cholinergic neurons: maintaining high hippocampal acetylcholine level by persistent firing during theta epochs, consequently suppressing ripples and allowing theta oscillations to dominate.

Key words: **acetylcholine; hippocampus; medial septum; muscarinic receptors; sharp wave-ripple**

Significance Statement

The major source of acetylcholine in the hippocampus comes from the medial septum. Early experiments found that lesions to the MS result in the disappearance of hippocampal theta oscillation, which leads to speculation that the septo-hippocampal cholinergic projection contributing to theta oscillation. In this article, by long-term recording of MS cholinergic neurons, we found that they show a theta state-related firing pattern. However, optogenetically activating these neurons shows little effect on theta rhythm in the hippocampus. Instead, we found that activating MS cholinergic neurons during slow-wave sleep could suppress hippocampal ripple oscillations. This suppression is mediated by muscarinic M_2 and M_4 receptors.

Introduction

Hippocampal local field potentials (LFPs) are associated with behavioral states. The most thoroughly studied hippocampal LFP oscillations include theta oscillation (4–12 Hz; Grastyán et al., 1959; Jouvet, 1969; Vanderwolf, 1969; Bland, 1986), gamma oscillation (30–80 Hz; Bragin et al., 1995), and ripple oscillation (100–250 Hz; Vanderwolf, 1969; Buzsáki, 1986). Theta oscillation occurs during animal active exploration (AE) and rapid eye movement (REM) sleep (Jouvet, 1969; Vanderwolf, 1969), representing an online encoding process of the animal (Buzsáki, 2002). High-frequency ripples are transient oscillations during behavioral immobility and slow-wave sleep (SWS; Buzsáki et al., 1992). Ripples are critical for memory consolidation, retrieval, and planning (Girardeau et al., 2009; Carr et al., 2011; Pfeiffer and Foster, 2013). Revealing the mechanism underlying the transition between these oscillations could lead to better understanding of different neural encoding schemes.

Lesion or pharmacological inactivation of medial septum and diagonal band of Broca (MS-DBB) completely abolishes theta throughout the hippocampus (Rawlins et al., 1979; Mizumori et al., 1990), which suggests that MS-DBB is critical in maintaining hippocampal theta oscillations. Histologic studies have shown that GABAergic neurons, cholinergic neurons, and glutamatergic

Received Aug. 5, 2019; revised Mar. 11, 2020; accepted Mar. 13, 2020.

Author contributions: X.M., L.L., and J.X. designed research; X.M., Y.Z., L.W. and N.L. performed research; X.M., Y.Z., X.Z., L.L., and J.X. analyzed data; and X.M., Y.Z., E.B., L.L., and J.X. wrote the paper.

*X.M. and Y.Z. contributed equally to this work.

This work was supported by the National Natural Science Foundation of China (Grant 31661143038 and 31800890), Shanghai Municipal Science and Technology Major Project (Grant No. 2018SHZDZX05), Shanghai Sailing program (17YF1426800), Shanghai Tongji University Education Development Foundation (to L.L.) and the the Israel Science Foundation (2523/16). We thank Dr. Guoping Feng (Massachusetts Institute of Technology) for generously sharing the ChATChR2-EYFP mouse line.

The authors declare no competing financial interests.

Correspondence should be addressed to Longnian Lin at lnlin@brain.ecnu.edu.cn or Jiamin Xu at xujiamin@bio.ecnu.edu.cn.

https://doi.org/10.1523/JNEUROSCI.1568-19.2020

neurons constitute the majority of MS-DBB neurons (Kiss et al., 1990; Hajszan et al., 2004). The major source of acetylcholine (ACh) in the hippocampus comes from the septo-hippocampal cholinergic system (Lewis et al., 1967; Sun et al., 2014; Li et al., 2018). Microdialysis and amperometric monitoring of hippocampal ACh reveal high ACh levels during theta states of the animal, in contrast to low ACh levels during non-theta states (Marrosu et al., 1995; Zhang et al., 2010; Teles-Grilo Ruivo et al., 2017), indicating a strong correlation between ACh and hippocampal theta oscillations.

Several studies have shown that ACh is involved in the transition between brain states. Activation of muscarinic ACh receptors (mAChRs) eliminates sharp-wave ripples (SWRs) in the mouse hippocampal CA1 region *in vitro* (Norimoto et al., 2012). Optogenetic activation of MS cholinergic neurons during SWS suppresses hippocampal ripple oscillations (Vandecasteele et al., 2014). Computational studies suggest an unbalanced excitation/inhibition behind such a suppression effect (Melonakos et al., 2019). But the neural mechanism underlying such a phenomenon is still elusive.

Despite the vital role of the septo-hippocampal cholinergic system on the transition of brain states, the *in vivo* firing patterns and physiological function of MS cholinergic neurons are yet to be characterized in freely behaving mice. Recordings from MS-DBB cholinergic neurons in head-fixed mice reveal that neurons with slow firing kinetics show higher firing rates during SWS than wakefulness, which is contrary to the conclusion of the ACh concentration studies (Simon et al., 2006). In the present study, we combined optogenetics with multichannel *in vivo* recordings and recorded simultaneously in the medial septum and hippocampus in choline acetyltransferase (ChAT)-channelrhodopsin-2 (ChR2)-enhanced yellow fluorescent protein (EYFP) transgenic mice. MS cholinergic neurons were identified by optogenetic tagging. We continuously recorded the activities of MS cholinergic neurons for long periods and further explored how optogenetic activation of MS cholinergic neurons influences hippocampal neural activities.

Materials and Methods

Subjects

ChAT-ChR2-EYFP transgenic mice were generated using a bacterial artificial chromosome (BAC) clone, as previously described (Zhao et al., 2011). Briefly, ChR2-EYFP, which contains the H134R mutation, was engineered into the ATG exon of the specific BAC clones through homologous recombination. ChAT-ChR2-EYFP line 6 was reported to show strong ChR2-EYFP expression in the striatum, basal forebrain, facial nucleus, trochlear nucleus, medial habenula, interpeduncular nucleus, and various other brainstem motor nuclei. For electrophysiological recordings from brain slices or immunostaining, we used adult ChAT-ChR2-EYFP mice (6–12 weeks old, 18–25 g) of either sex. For recordings *in vivo*, we used adult male ChAT-ChR2-EYFP mice (10–20 weeks old, 22–30 g). All procedures were approved by the Animal Advisory Committee at East China Normal University (No. AR201404008) and were performed in accordance with the National Institutes of Health *Guidelines for the Care and Use of Laboratory Animals.*

Immunohistochemistry and confocal imaging

Anesthetized mice were perfused with 100 mM PBS, pH 7.4, followed by cold 4% paraformaldehyde in PBS. After perfusion, the brains were removed, fixed for another 18 h, and transferred to a 10–30% sucrose solution. Finally, 30-μm-thick sections were prepared on a freezing microtome (Leica). Every third section was taken from the region between the bregma + 1.2 mm and + 0.3 mm. Sections were rinsed with 0.3% Triton X-100 in 0.1 M PBS and were blocked with 4% normal bovine serum for 1 h, followed by incubation with primary antibodies including goat anti-ChAT (1:200; Millipore) and mouse anti-GFP (1:500; Millipore) for 12 h at 4°C. Sections were then washed with PBS-T and incubated with secondary antibodies including Cy3-conjugated donkey anti-goat (1:500; Jackson ImmunoResearch) and Invitrogen Alexa Fluor 488 donkey anti-mouse (2 mg/ml; Thermo Fisher Scientific) for 3 h at room temperature. Finally, sections were washed and mounted with DAPI (1:50,000). Then sections were mounted with DAPI-containing 50% glycerol. Images were acquired by a scanning confocal microscope (A1R, Nikon Instruments).

Brain slice preparation and electrophysiological recordings

The 300-μm-thick coronal slices were cut from 6-week-old mice with a vibratome in ice-cold cutting solution containing 87 mM NaCl, 3 mM KCl, 0.5 mM $CaCl_2$, 7 mM $MgSO_4$, 1.25 mM NaH_2PO_4, 25 mM $NaHCO_3$, 10 mM D-glucose, 60 mM sucrose, 1.3 mM sodium ascorbate, and 0.6 mM sodium pyruvate. Slices were then maintained in artificial CSF (aCSF) containing 125 mM NaCl, 3 mM KCl, 2 mM $CaCl_2$, 2 mM $MgSO_4$, 1.25 mM NaH_2PO_4, 25 mM $NaHCO_3$, 10 mM D-glucose, 1.3 mM sodium ascorbate, and 0.6 mM sodium pyruvate saturated with 95% O_2 and 5% CO_2 at 34°C for 30 min, and then transferred into a recording chamber on an upright fluorescent microscope. During recording, slices were submerged and superfused (2 ml/min) with aCSF at room temperature (22–25°C).

ChR2-EYFP-expressing neurons were visualized under a fluorescent microscope (BX51WI, Olympus) equipped with both differential interference contrast optics and a filter set for visualizing EYFP using a 40× water-immersion objective and a charge-coupled device camera. Whole-cell recordings were made using an electrode solution containing 125 mM K-gluconate, 2 mM KCl, 10 mM Na-phosphocreatine, 10 mM HEPES, 0.5 mM EGTA, 4 mM Mg-ATP, and 0.3 mM Na-GTP, pH 7.3 and 290 mOsm/L; in experiments recording the IPSCs, KCl was used to replace potassium gluconate.

Microdrive array assembly

The recording microdrive array contained an optrode bundle for MS and a tetrode bundle for CA1, adapted from our previous study (Lin et al., 2006). The two bundles could be driven independently by rotation of the screws, with each full turn corresponding to 280 μm in depth penetration. In detail, a foundation of the recording microdrive was prepared by assembling a printed circuit board base, screws and nuts. Then two 36-pin connectors (NPD-36-VV-GS, Omnetics) were attached to the foundation by epoxy. The tetrodes were constructed from four twisted 13-μm-diameter nichrome wires (California Fine Wire) bound together by melting their insulation (Czurkó et al., 2011), with gold-plated tips to reduce the electrode impedance to 500–800 KΩ at 1 kHz. The optrode bundle has eight tetrodes surrounding a 200-μm-diameter optic fiber [numerical aperture (NA) = 0.39; Thorlabs]. The recording end of the tetrodes extended ~0.5 mm beyond the tip of the optical fiber, and the other end of the tetrodes was wired to pins of the connector.

Implantation surgery

A mouse was anesthetized with pentobarbital sodium (40 mg/kg) and mounted into the stereotactic frame (Stoelting). The body temperature of the mouse was kept constant by a small-animal thermoregulation device (FHC). The scalp was shaved, and the skull was exposed under antiseptic conditions. The optrodes/tetrodes were implanted at an angle of 10° to avoid damage of the superior sagittal sinus above MS. In detail, two positions (0.8 mm anterior and 0.6 mm lateral to bregma for MS; and 2.3 mm posterior and 2.0 mm lateral to bregma for CA1) were measured and marked, and then small craniotomies were made at these positions. After removal of the dura, the wired microdrive was positioned at an angle of 10° and slowly lowered so that the optrodes and tetrodes went through the craniotomies until the optrodes in MS reached a depth of ~2.7 mm and the tetrodes in hippocampus reached a depth of ~0.7 mm. The gaps between the electrodes and craniotomies were filled with softened paraffin, and the microdrive was secured on the skull with dental cement and screws. The ground wire was soldered to a screw mounted on the skull above the cerebellum. A piece of copper mesh was wrapped around the entire microdrive, serving as a Faraday

cage as well as protecting the wires from potential scratching damage. After surgery, animals were separately housed in plastic buckets (55 cm diameter, 42 cm height), with free access to food and water, on a 12 h light/dark cycle. Animals were allowed to recover for 1 week.

In vivo recording in freely behaving mice

The connectors on the microdrive were plugged into preamplifiers with extended cables to monitor neuronal signals using the Plexon MAP system (the optic fiber on the microdrive was connected to a laser with an optical patch cable). To enable the mouse to move freely, a helium-filled mylar balloon was tied to the cables for alleviating the weight of the apparatus and cables. The extracellular signals from electrodes were filtered through the preamplifiers to separate neuronal activity and local field potentials. The spike signals (sampling at 40 kHz) and the LFP signals (sampling at 1 kHz) were filtered online at 400–7000 and 0.7–300 Hz, respectively. Spike waveforms, time stamps, and LFP signals were saved to Plexon data (*.plx) files. The MS optrodes and hippocampal tetrodes were advanced manually every day until the optrode-detected neuronal firings responded to optical stimulation and the hippocampal tetrodes reached the CA1 pyramidal layer, which was deduced from LFP characteristics and neuronal activity patterns.

After the experiments, histologic staining of brain slices with 1% cresyl violet was used to confirm the electrode positions.

Optical stimulation delivery

For optical stimulation during brain slice recording, light was generated by a 473 nm laser (Shanghai Dream Lasers Technology) and delivered through an optical fiber (200 μm core diameter; NA = 0.39; Thorlabs) that was submerged in aCSF and placed ~300 μm above the recording site. Square light pulses were controlled by transistor–transistor logic (TTL) modulation.

For optical stimulation during *in vivo* recording, light was also generated by a 473 nm laser (Shanghai Dream Lasers Technology). Patterns of optical stimulation were controlled by TTL modulation. Square pulses 5 ms in length were delivered at different frequency. Light power at the end of the optrodes were ~30 mW/mm^2. For optical stimulation of firing reliability test, we used 20 pulses per train and repeated two to five trains at each frequency. For optical stimulation of suppressing ripple oscillations, we used 10 Hz train pulses lasting 50 s if not otherwise mentioned.

Behavioral recording

Video recordings of animal behaviors were obtained via a ceiling mounted camera at 30 frames per second and synchronized with electrophysiological recordings. Most of the behaviors, such as sleeping, eating, and quiet waking, were recorded in plastic buckets (55 cm diameter, 42 cm height) where the mouse was held after surgery, while waking exploration experiments were conducted in a square box (40 × 40 × 20 cm) enriched with toys.

Intraperitoneal injection and microinjection

Mice were intraperitoneally injected with atropine sulfate (5 mg/ml) at 25 mg/kg body weight and mecamylamine (MEC; 2 mg/ml) at 10 mg/kg body weight. For microinjection, a guide cannula (inner diameter = 200 μm; outer diameter = 400 μm) was implanted into hippocampal dorsal CA1 (anteroposterior: −2.3 mm; mediolateral: 1.2 mm; dorsoventral: −1.3 mm), ipsilateral to the recording microdrive. A 1.5-m-long polyimide tubing was attached to an injection cannula (inner diameter = 75 μm; outer diameter = 150 μm), enabling the mouse to behave freely in the recording apparatus. A 1 μl Hamilton microsyringe was connected to the other end of the tubing. We filled the injection cannula and polyimide tubing with drug solution before the recording started. Then we replaced the dummy in the guide cannula with the injection cannula. Drug was injected in a 1 μl volume over a 10 min period under the control of a syringe pump (Stoelting) while the animal was freely behaving during electrophysiological recording. Atropine sulfate (0.5, 2.5, 5, and 10 μg; Honda et al., 2004), VU0255035 (2.5 and 5 μg; Sheffler et al., 2009; Kurowski et al., 2015; Miller et al., 2017), (*S*)-(+)-dimethindene maleate (DiM; 13, 26, and 39 μg; Pfaff et al., 1995; Lambrecht et al., 1999; Yang et al., 2017), J104129 fumarate (25 and 50 μg; Bader and Diener, 2015; Tsentsevitsky et al., 2017), and tropicamide (2, 4, and 8 μg; Lazareno et al., 1990; Hernández et al., 1993; Veeraragavan et al., 2011) were administered respectively in different groups. The injection cannula was left in place until the recording ended.

Spike sorting

Individual neurons were sorted by clustering methods in Offline Sorter software (Plexon), performed manually in a three-dimensional feature space.

Detection of theta, gamma, and ripple oscillations

To detect theta oscillations, a theta (5–10 Hz)/delta (2–4 Hz) ratio was calculated by sliding a 2 s window after the original LFP was bandpass filtered at 4–12 Hz. Epochs with more than three consecutive time windows in which the ratio was >4 were identified as theta episodes (Csicsvari et al., 1999). REM sleep was recognized by characteristic theta oscillations and video verification of sleeping of the animal.

To detect gamma oscillations, the original LFP was digitally bandpass filtered (30–80 Hz). Gamma power [root mean square (RMS)] of the filtered signal was calculated by sliding a 25 ms window every 1 ms, and the threshold of detecting gamma episodes was set to 2 SDs above the background mean power (Csicsvari et al., 2003).

To detect ripple oscillations, the original LFP was digitally bandpass filtered (100–250 Hz). The power (RMS) of the filtered signal was calculated by sliding a 10 ms window every 1 ms. Epochs with 5 SDs above the background mean power were designated as ripple episodes. Then the time window was moved forward and backward to detect the beginning and the end of each ripple episode, the threshold was 2 SDs above the background mean power (Csicsvari et al., 1999; Klausberger et al., 2003).

Ripple events inhibition index was calculated as follows:

$$\text{Ripple event inhibition index} = (N_{\text{off}} - N_{\text{on}})/N_{\text{off}} \times 100\%,$$

where N_{off} is the number of ripple events in the 50 s time window before light stimulation, and N_{on} is the number of ripple events happened during the 50 s light stimulation.

Power spectrum analysis

An augmented Dickey–Fuller test was applied to select stationary data for further analysis. A power spectral density analysis was performed on LFP signals using Welch's averaged periodogram method with a 1024 ms nonoverlapping Hanning window (NFFT = 2048). Time–frequency representations of LFPs was performed using short-time Fourier transform in overlapping 512 ms Hanning window with a step size of 50 ms (NFFT = 512). Theta power is defined as the mean LFP power in theta band (4–12 Hz), and ripple power is the mean LFP power in ripple band (140–250 Hz).

Ripple power inhibition index was calculated as follows:

$$\text{Ripple power inhibition index} = (P_{\text{off}} - P_{\text{on}})/P_{\text{off}} \times 100\%,$$

where P_{off} is the mean LFP power in ripple band (140–250 Hz) in the 50 s time window before light stimulation, and P_{on} is the mean LFP power in ripple band during the 50 s light stimulation period.

Theta-correlated firing analysis

Each recording was binned into 10 s windows. The theta score of LFP and the firing rate of a cholinergic neuron were calculated within each window. The LFP was downsampled to 200 Hz, and then a power spectrum analysis was performed. The theta score was defined as the ratio of the power in theta band (4–12 Hz) to the power in slow-wave band (0.5–4 Hz). The Spearman correlation coefficient was calculated between the theta score of the LFP and the firing rate of the neuron.

Table 1. Animal number in different experiments

Experiments	*n*
In vivo recording of cholinergic neurons	16
Optogenetic stimulation	10
Intraperitoneal injection	6
Atropine	5
MEC	6
Hippocampal microinjection	11
Atropine	5
DiM	5
Tropicamide	5
VU0255035	2
J102149	3

Phase-locking firing analysis

The theta-filtered (4–12 Hz) or gamma-filtered (30–80 Hz) LFP $y(t)$ was first decomposed into instantaneous amplitude $\rho(t)$ and phase $\phi(t)$ components as follows:

$$y(t) = Re(\rho(t)e^{j\phi(t)})$$

by using a Hilbert transform. Then, given the spike train $\{t_i | i = 1, 2, \ldots, n\}$, the spike phase was calculated as follows:

$$\varphi_i = \varphi(t_i).$$

To evaluate the presence of phase locking, a Rayleigh's test (periods during which cells fired <50 spikes were excluded) for circular uniformity was performed to compute the significance ($p < 0.05$) of phase locking and corresponding preferred phases (Siapas et al., 2005). The unit phase was fit with a von Mises distribution.

Data and software availability

Data were analyzed by built-in or custom-built MATLAB (MathWorks) scripts. The data and MATLAB scripts that support the findings of this study are available from the corresponding authors on request.

Experimental design and statistical analyses

We used a total of 27 male ChAT-ChR2-EYFP transgenic mice in our study. The number of mice used in different experiments is listed in Table 1. For *in vivo* recording of cholinergic neurons, optogenetic stimulation and intraperitoneal injection experiments, we used a total of 16 mice. They had an optrode bundle implanted in the MS and a tetrode bundle implanted in CA1. For the 11 mice used for microinjection, an additional injection cannula was implanted in ipsilateral CA1. Note that due to experimental difficulties, some mice participated in multiple experiments (e.g., two mice injected with VU0255035 were also used for J102149 injection). For mice that participated in multiple injections, the interval between injections was at least 3 d.

Detailed statistical analysis can be found in the corresponding descriptions of the results. Generally, data are presented as the mean ± SD. Comparisons between two groups were tested by *t* test. Multiple comparisons were conducted by Bonferroni correction or one-way ANOVA with *post hoc* Holm–Sidak test. Statistical significance was set at $p < 0.05$. Multiple comparisons of correlation coefficient and theta phase locking were conducted by Pearson test and Rayleigh's test with Bonferroni correction; to be specific, the final *p* value is the largest *p* value of all the individual comparisons multiplied by the number of comparisons (Prince et al., 2013; Seki and Tomyta, 2019; Shen et al., 2019). Multiple comparisons of the gamma phase locking were conducted by Rayleigh's test with false discovery rate (FDR) test. Multiple comparisons of ripple inhibition were conducted by one-way ANOVA with *post hoc* Holm–Sidak test.

Results

Expression and functionality of ChR2 in MS cholinergic neurons *in vitro*

We first examined ChR2 expression on MS cholinergic neurons in the constructed ChAT-ChR2-EYFP transgenic mouse. Colocalization of ChR2-EYFP and ChAT was apparent in medial septum, with ChR2-EYFP expressed on cell membrane and ChAT expressed in cytoplasm (Fig. 1*A*). In the medial septum, a lot of cholinergic neurons expressed ChR2-EYFP (72.1 ± 10.4%), while most ChR2-EYFP-positive neurons expressed ChAT (98.3 ± 3.4%; Fig. 1*B*; $n = 5$ mice). Furthermore, ChR2-ChAT coexpressing axon terminals were present in dorsal CA1 area of the hippocampus. The most abundant ChAT-ChR2 innervations were in stratum pyramidale (Fig. 1*C*).

To test the physiological function of ChR2 on cholinergic neurons, we first performed *in vitro* patch-clamp recording in ChAT-ChR2-EYFP mouse brain slices containing the medial septum. We recorded nine ChR2-EYFP-positive neurons from six slices ($n = 3$ mice). Holding the membrane potential at −50 mV in voltage-clamp mode, we observed depolarization of the membrane potential and slow-firing activities with spike accommodation of the neuron on 350 pA current injection (Fig. 1*D*), which is consistent with published results (Sotty et al., 2003; Simon et al., 2006). We also observed large-amplitude inward currents with peak amplitude at 532.0 ± 171.4 pA when blue light stimulation (473 nm, 10 mW/mm^2) was delivered under voltage-clamp mode ($n = 4$ neurons; Fig. 1*E*). A light stimulation frequency of 10 Hz (5 ms pulse) faithfully induced spiking activities of the recorded neuron under current-clamp mode (Fig. 1*F*). The induced spikes reliably followed the light pulses at different light stimulation frequency under 20 Hz. The reliability of light-evoked firing activities dropped gradually with the increase of light stimulation frequency >20 Hz (Fig. 1*G*). The induced firing reliability decreased to <50% following 50 Hz light stimulation (32 ± 24%, $n = 4$ neurons; Fig. 1*G*). In addition, the latency of the evoked spike onset increased gradually within each train of light pulse stimulation, with a more prolonged spike latency at higher stimulus frequency. This could be related to the intrinsic ChR2 light adaptation process and a decrease in membrane repolarization level between spikes (Grossman et al., 2011).

Optogenetic tagging of MS cholinergic neurons *in vivo*

We customized microdrive tetrode arrays for simultaneous optrode recording in the medial septum and tetrode recording in the pyramidal layer of dorsal CA1 area of the hippocampus in freely behaving ChAT-ChR2-EYFP mice. Each bundle of eight tetrodes in an array was designed to be independently drivable. A 200-μm-diameter optic fiber was assembled in the center of the MS tetrode bundle, forming an optrode. Thus, we could deliver light stimulation to the recorded medial septum neurons (Fig. 2*D*). MS neurons were identified as cholinergic neurons based on light-induced spike responses (Fig. 2*A*,*B*).

We recorded a total of 61 neurons from the medial septum in six male ChAT-ChR2-EYFP transgenic mice. Among these recorded neurons, we identified seven cholinergic neurons, with five cells recorded from five mice, respectively, and the other two cells recorded from the other animal (Fig. 2*B*,*E*, M14SC06 and M14SC08). The waveforms of the light-evoked spikes resembled the waveforms of spontaneous spikes (Fig. 2*B*,*E*; Pearson test with Bonferroni correction for seven neurons: $p = 5.70\text{e-}95$). Similar to our recordings from brain slices, the reliability of *in vivo* light-evoked neuronal responses decreased with the progression of light stimulus frequency (Fig. 2*C*). The light-evoked spike

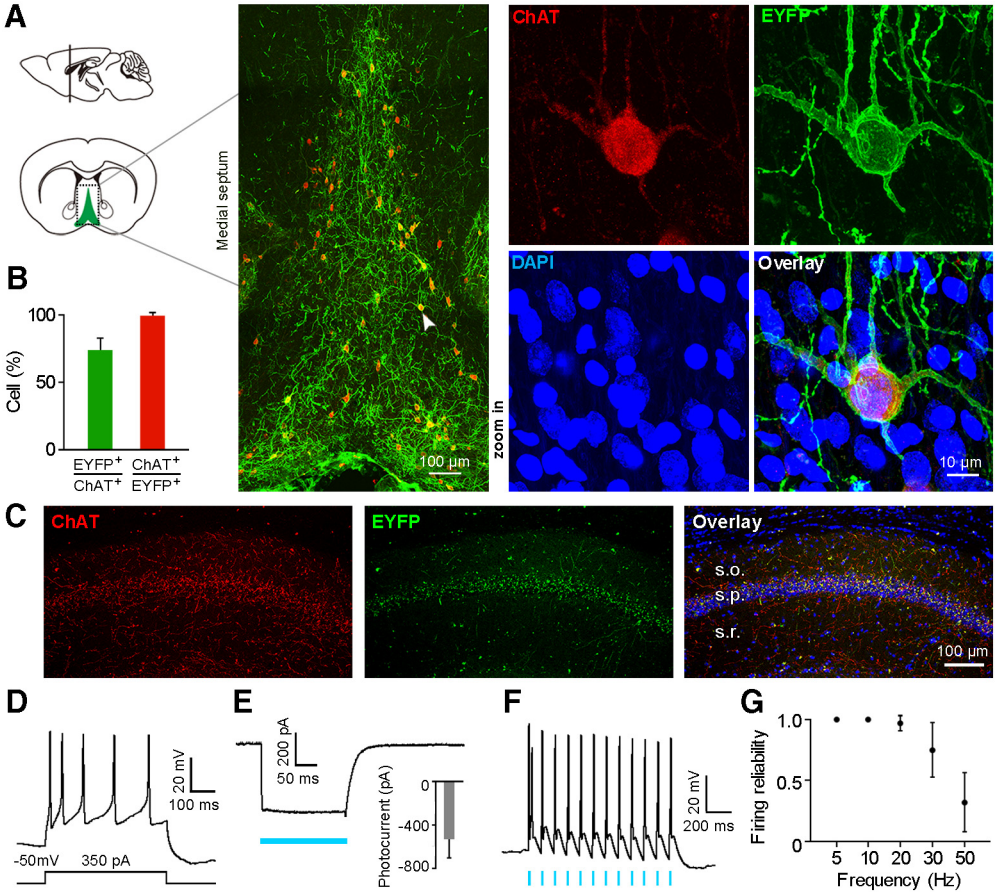

Figure 1. ChR2 is strongly expressed in MS cholinergic neurons and mediates robust optogenetic activation in ChAT-ChR2-eYFP transgenic mice. ***A***, Left, Schematic drawing shows MS in a coronal plane. Middle, Confocal image of boxed area on the left shows that ChR2-eYFP (green) is strongly expressed in ChAT-positive neurons (red). The neuron indicated by the arrowhead is shown at right in the high-magnification view. ***B***, Percentages of ChAT neurons that are ChR2-eYFP positive, and vice versa (mean ± SD; $n = 5$ mice). ***C***, Confocal image of a hippocampal coronal section shows cholinergic terminals colocalized with ChR2-EYFP in the hippocampal CA1 area, with the most abundant innervations found in stratum pyramidale. ***D***, Action potentials induced by current injection in a ChR2-EYFP-expressing neuron from a brain slice patch-clamp recording. ***E***, Blue light-evoked photocurrent in a ChR2-positive neuron under voltage-clamp mode (membrane potential was held at −50 mV). Inset, Average light-evoked currents in these neurons (−532 ± 171.4 pA, mean ± SD; $n = 4$ neurons). ***F***, Action potentials evoked by 10 Hz blue light pulses (5 ms pulse width) from a ChR2-positive cholinergic neuron. ***G***, Firing fidelity of light-evoked spikes at different light stimulation frequencies (mean ± SD; $n = 4$ neurons; 5 ms pulse width).

reliability was 0.35 ± 0.37 ($n = 7$ neurons) under 50 Hz light stimulus frequency. Based on the optogenetic tagging results, we confirmed that the seven neurons recorded from the medial septum of ChAT-ChR2-EYFP transgenic mice were cholinergic neurons.

Theta state-related firing of MS cholinergic neurons in freely behaving mice

We continuously recorded these identified MS cholinergic neurons for 5.5–72 h, together with video monitoring of animal behavior. The length of recording periods varied, because the length of recordable periods of the neurons differed. We were able to continuously monitor 3 MS cholinergic neurons for >24 h). Among the seven cholinergic neurons, six of them showed similar firing patterns. Figure 3*A* shows continuous *in vivo* firing profile of a MS cholinergic neuron in one circadian cycle (24 h). The firing rate of this neuron never exceeded 10 Hz during any of the indicated behavior states (2 s time bin), with the highest firing rate at 9.5 Hz during the AE state (Fig. 3*A*, red star; ~12.5 h). The peak firing rates of these six MS cholinergic neurons ranged from 7.5 to 15 Hz, with an average firing rate of 10.92 ± 2.87 Hz ($n = 6$ neurons). Large firing rate peaks occurred during the theta-dominant periods.

MS cholinergic neurons showed tonic firing that correlated with brain activity states. They were highly active during theta states (average firing rate during AE: 7.33 ± 1.41 Hz; average firing rate during REM sleep: 3.90 ± 1.16 Hz; $n = 6$ neurons), but were almost silent during non-theta states (average firing rate during SWS: 0.12 ± 0.07 Hz; $n = 6$ neurons). They could even go several minutes without one single spike. To evaluate the correlation between cholinergic neuronal firing and hippocampal theta states, we defined theta score as LFP theta power divided by slow-wave power. The firing activities of MS cholinergic neurons correlated with hippocampal LFP theta scores (Fig. 3*A*). Figure 3*B* shows enlarged views of the boxed areas in Figure 3*A*, which illustrate in detail the temporal coupling between the firing of the MS cholinergic neuron and hippocampal theta when the behavior state of the animal changed. These state changes include the following: quiet waking to AE (Fig. 3*B*, 1); AE to quiet waking (Fig. 3*B*, 2); AE with wheel running (Fig. 3*B*, 3); and SWS intermingled with REM sleep (Fig. 3*B*, 4). Further analysis revealed a strong correlation between the firing rates of the example MS cholinergic neuron and LFP theta score (Fig. 3*C*; Pearson test with Bonferroni correction for six neurons: $R = 0.77 \pm 0.05$, $p = 7.72\text{e-}11$). The average firing rate of the six neurons shows a similar decreased tendency with hippocampal

theta score (Fig. 3*D*). Furthermore, the firing activities of the six MS cholinergic neurons were phase locked to hippocampal theta oscillations (Rayleigh's test with Bonferroni correction for six neurons: $p = 0.04$). Figure 3*E* shows phase-locked firing of one example neuron to hippocampal theta oscillation (Rayleigh's test, $p = 1.4e\text{-}29$), but not to gamma oscillations (Rayleigh's test, $p = 0.1$; Fig. 3*F*; Rayleigh's test with FDR correction for six neurons: $p = 5.5$).

MS cholinergic activation suppressed ripple oscillation in hippocampal CA1

We have shown that the *in vivo* firing of MS cholinergic neurons is strongly correlated with hippocampal theta oscillations. To further investigate this relationship, we tried to quantify the impact of optogenetically activating MS cholinergic neurons on hippocampal neuronal activities during different behavior states. Since MS cholinergic neurons were less active during SWS, we first delivered 10 Hz blue light stimulation with 5 ms pulse width for 50 s to the MS in ChAT-ChR2-EYFP transgenic mice during SWS. MS cholinergic neurons were activated and fired at ~10 Hz (Fig. 4*A*). During the stimulation period, there was no obvious evidence of hippocampal theta oscillations (theta score changed from 0.72 ± 0.26 to 0.75 ± 0.16; $n = 6$ mice; paired t test, $p = 0.74$, $t = 0.36$). But we observed a significant change on hippocampal theta power as it decreased from 0.59 ± 0.17 to 0.41 ± 0.12 (mean ± SD; $n = 6$ mice; one-way ANOVA, $p = 0.029$, *post hoc* Holm–Sidak test, $p = 0.015$, $t = 4.8$; Fig. 4*B*). Interestingly, hippocampal ripple oscillations were almost completely abolished (Fig. 4*A*,*B*; mean ± SD: ripple power during SWS, $1.9e\text{-}3 \pm 0.7e\text{-}3$ mV^2; ripple power during light stimulation periods, $0.7e\text{-}3 \pm 0.2e\text{-}3$ mV^2). Ripple oscillations also diminished during the theta-dominant REM sleep state (ripple power during REM, $1.2e\text{-}3 \pm 0.5e\text{-}3$ mV^2). With the increase of spontaneous activities of MS cholinergic neurons as REM sleep progresses, hippocampal ripple oscillations were gradually suppressed (Fig. 4*A*,*B*). Beginning with the transition of REM sleep to SWS, the firing activities of MS cholinergic neurons decreased and ripple oscillations reappeared (Fig. 4*A*). Additional experiments revealed that the higher the optical stimulation frequency we used, the more activated the MS cholinergic neurons were, and hence the more suppressed the hippocampal ripple oscillations were (Fig. 4*C*,*D*). A stimulus frequency as low as 0.5 Hz could cause hippocampal ripple inhibition (ripple events inhibition index, $30 \pm 13\%$; $n = 7$ mice). However, there was no significant difference in the suppression of ripples between stimulation frequencies of 10 and 20 Hz (Fig. 4*D*; $n = 7$ mice; one-way ANOVA, $p = 3.8e\text{-}8$; *post hoc* Holm–Sidak test, $p = 0.30$, $t = 1.79$). These results indicate that the cholinergic suppression of hippocampal ripples depends on the light-evoked firing of MS cholinergic neurons when the light stimulation frequency is between 0.5 and 10 Hz (Fig. 4*D*).

Next, we tested the impact of the light activation of MS cholinergic neurons on hippocampal oscillations during theta-dominant AE and REM sleep states. Considering that the baseline activities of MS cholinergic neurons are relatively higher under these behavior states than SWS states (average firing rate during

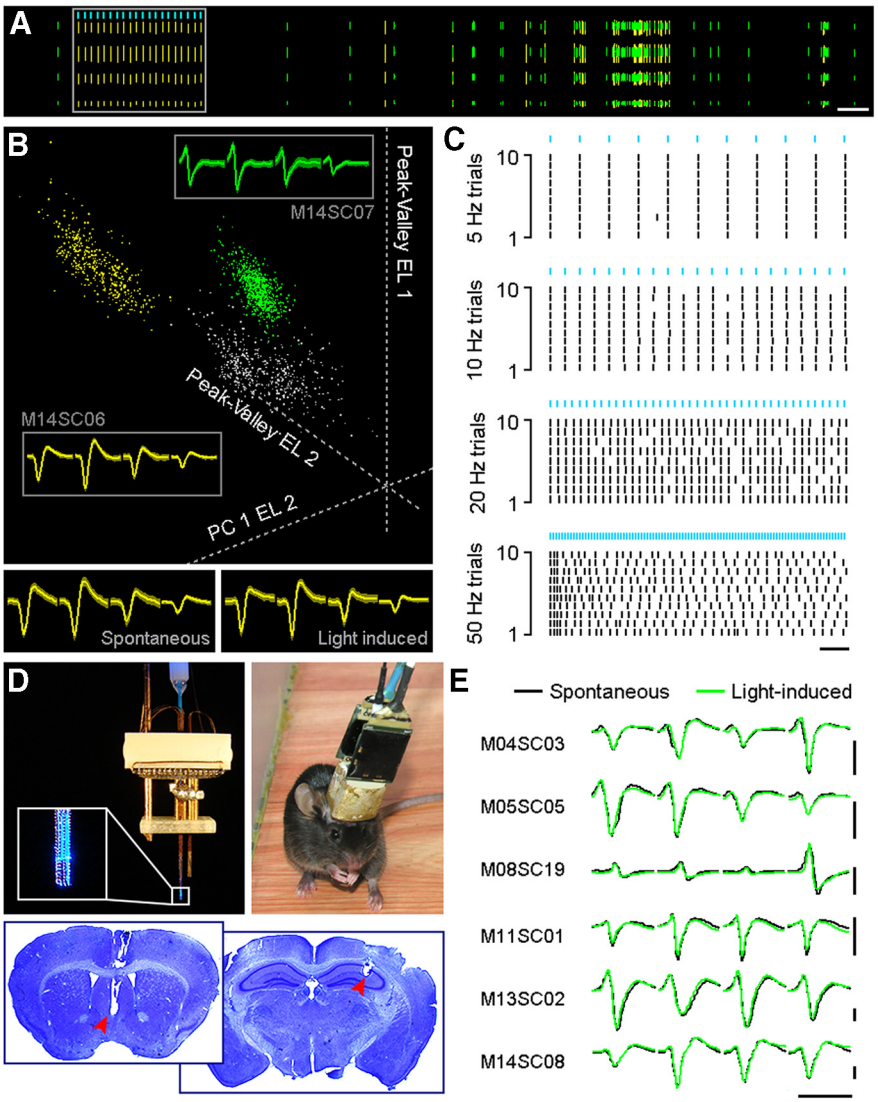

Figure 2. *In vivo* optogenetic tagging of MS ChAT-ChR2 neurons. ***A***, Spike activities of a representative ChAT-ChR2 neuron (yellow ticks) recorded with tetrodes in a freely behaving mouse. Spike waveforms of two simultaneously recorded units (yellow and green) from one tetrode are shown. Ticks in each row represent waveform sequences recorded by one channel of the tetrode. Light-induced spikes are illustrated in the boxed area. Calibration: 5 s. ***B***, Cluster separation of the two neurons depicted in ***A*** (yellow and green) in a 3D feature space. Average tetrode waveforms are shown in the gray boxed area with neuron identities labeled outside the box. Average waveforms of spontaneous and light-induced spikes are illustrated separately at the bottom. ***C***, Raster plot activity of the entrained ChAT-ChR2 neuron in response to different optogenetic stimulation frequencies (5 ms pulses, blue bars). Calibration: 20 s. ***D***, Top left, A microdrive recording array connected to a laser generator. Enlarged box shows the tip of the optrode. Top right, A ChAT-ChR2-EYFP mouse after recovery from electrode implantation surgery. Bottom, Electrode recording sites revealed by Nissl staining. Red arrowheads indicate the tips of the electrode bundles. ***E***, Spontaneous and light-induced waveforms of six MS ChAT-ChR2 neurons recorded by tetrodes, not including the neuron shown in ***B*** (M14SC06). No significant change in waveforms is observed between spontaneous and light-induced spikes. Calibration: 1 ms, 0.2 mV.

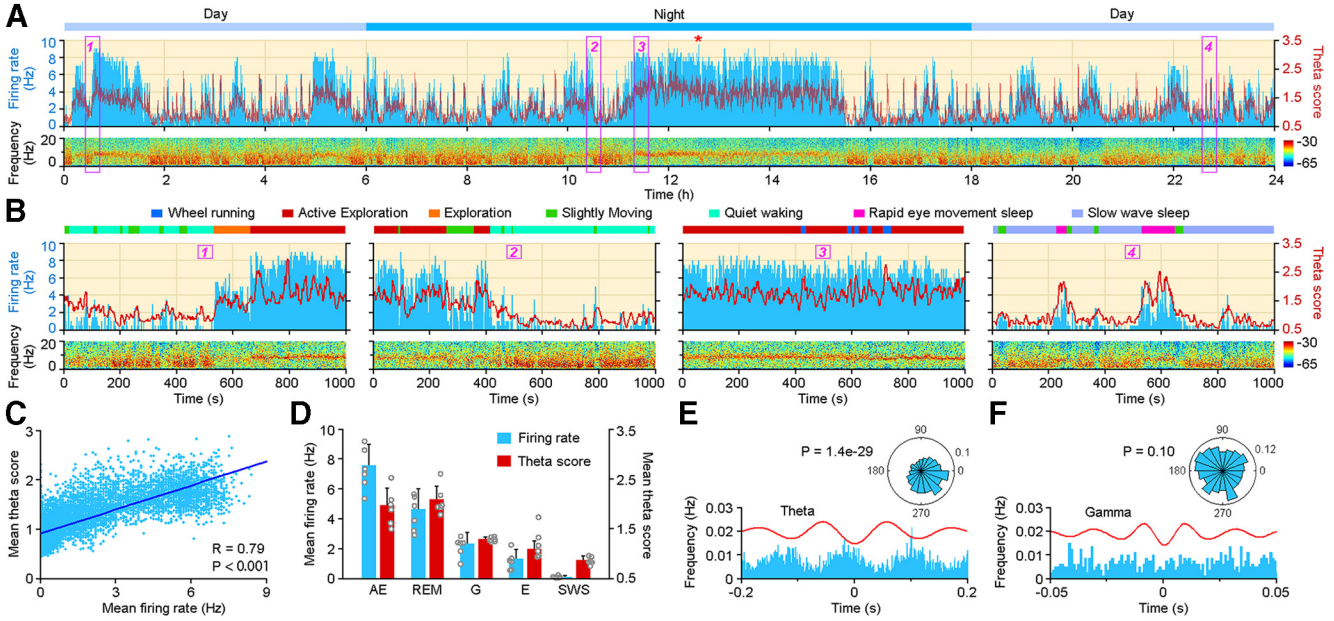

Figure 3. Spontaneous *in vivo* Firing Pattern of MS ChAT-ChR2 Neurons. ***A***, Twenty-four hour recording of an MS ChAT-ChR2 neuron (M13SC02) shows that the ups and downs of firing activities (top, blue histogram) coincide with a theta score of the simultaneously recorded CA1 LFP (top, red trace). Power spectrogram of the LFP is illustrated at the bottom. The recording started at noon and lasted for 24 h. Four boxed areas are enlarged in ***B***. ***B***, Zoomed-in representations of the boxed area in ***A***. Note the temporal coupling of neuronal firing (blue histogram) and LFP theta score (red trace) under different behavior states. Color bars indicating different behaviors are illustrated on top of each plot. ***C***, LFP theta score is correlated with the firing rate of the MS ChAT-ChR2 neuron (the 24 h recording in ***A***; Pearson test with Bonferroni correction, $R = 0.79$, $p = 0$). ***D***, Mean firing rate of the six MS ChAT-ChR2 neurons and theta score of CA1 LFP during different behavior states (each dot represents one neuron; mean ± SD). G, Grooming; E, eating. Both the mean firing rate and the theta score show high values during theta dominance (AE and REM) and low values during SWS. ***E***, Phase relations between firing of the MS ChAT-ChR2 neuron (M13SC02) and CA1 LFP theta. Bottom, Discharge frequency of the MS ChAT-ChR2 neuron aligned to the theta trough (red line, averaged theta oscillation). Top, Preferred firing phase of the ChAT-ChR2 neuron during theta oscillation. The neuron increased its firing probability around the trough of the theta cycle (Rayleigh's test, $p = 1.4e\text{-}29$). ***F***, Same as ***E***, but for phase relations with gamma oscillation. No significant phase locking with gamma oscillation was observed (Rayleigh's test, $p = 0.1$).

AE, 7.33 ± 1.41 Hz; average firing rate during REM sleep, 3.90 ± 1.16 Hz), we therefore chose a higher optical stimulation frequency of 20 Hz. We observed no significant impact on hippocampal theta frequency or power when 20 Hz optical stimulation was delivered either during AE (Table 2; $n = 9$ trials; paired t test: theta frequency, $p = 1$, $t = 5.57e\text{-}7$; theta power, $p = 0.96$, $t = 0.06$) or REM sleep (Table 2; $n = 9$ trials; paired t test: theta frequency, $p = 0.27$, $t = 1.18$; theta power, $p = 0.42$, $t = 0.85$). There is also no change on gamma power during AE (Table 2; $n = 9$ trials; paired t test: $p = 0.26$, $t = 1.21$) or REM state (Table 2; $n = 9$ trials; paired t test: $p = 0.1$, $t = 1.86$) between light-on and light-off periods.

MS cholinergic activation suppressed ripple oscillations via muscarinic acetylcholine receptors

There are two types of acetylcholine receptors in the CNS, muscarinic and nicotinic ACh receptor (nAChR). To further study the mechanism under ripple suppression effect caused by activating MS cholinergic neurons, we intraperitoneally injected the mAChR antagonist atropine (Fig. 5*A*) or the nAChR antagonist mecamylamine (Fig. 5*C*). Cholinergic suppression of hippocampal ripple oscillations was disrupted after intraperitoneal injection of atropine, but not of MEC (Fig. 5). Injection of atropine decreased the ripple events inhibition index from 95 ± 5% to 21 ± 22% (Fig. 5*B*; $n = 5$ mice; paired t test: $p = 1.7e\text{-}3$, $t = 7.44$). Atropine also decreased the ripple power inhibition index from 65 ± 11% to 17 ± 16% (Fig. 5*B*; $n = 5$ mice; paired t test: $p = 2.0e\text{-}3$, $t = 7.16$). There is no significant change after intraperitoneal injection of MEC (ripple events inhibition index changed from 86 ± 12% to 83 ± 17%; Fig. 5*C*,*D*; $n = 6$ mice; paired t test: $p = 0.54$, $t = 0.65$; ripple power inhibition index changed from 59 ± 14% to 53 ± 18%, Fig. 5*C*,*D*; $n = 6$ mice; paired t test: $p = 0.22$, $t = 1.41$). These results indicate that intraperitoneal injection of atropine successfully rescued ripple oscillations from being suppressed by light stimulation. The suppression of hippocampal ripples by optogenetic activation of MS cholinergic neurons was mediated by mAChRs, but not nAChRs.

When intraperitoneally injected, atropine acts on the mAChRs throughout the whole animal body. To overcome this limitation and further confirm whether hippocampal mAChRs indeed mediated the cholinergic suppression of ripple, we implanted a microinjection cannula in the dorsal CA1 area of the hippocampus in ChAT-ChR2-EYFP mice. Intrahippocampal injection of atropine (10 μg/μl, 1 μl total injection volume over 10 min) also weakened the ripple suppression effect caused by optical activation of MS cholinergic neurons. Furthermore, we confirmed that atropine rescue of ripple oscillation is dose dependent, with a higher dose of atropine resulting in less cholinergic suppression of ripple oscillations. The ripple event inhibition index is 88 ± 12% for control; and 83 ± 8% for 0.5 μg, 65 ± 19% for 2.5 μg, 26 ± 5% for 5 μg, and 12 ± 27% for 10 μg injection doses ($n = 8$ trials from two mice for each dose; one-way ANOVA, $p = 5.6e\text{-}6$; *post hoc* Holm–Sidak test: $p = 6.99e\text{-}6$, $t = 5.28$ for control vs 10 μg). There is no significant change of ripple incidence in the absence of light stimulation on atropine microinjection (with a 10 μg injection dose, ripple incidence changed from 0.36 ± 0.22 Hz before atropine injection to 0.35 ± 0.16 Hz after the injection; $n = 15$ trials from two mice; t test: $p = 0.98$, $t = 0.08$).

MS cholinergic activation suppressed ripple oscillations via muscarinic M_2 and M_4 receptors

mAChRs are G-protein-coupled metabotropic receptors including five subtypes: M_1 to M_5. M_1 to M_4 subtypes are found in the

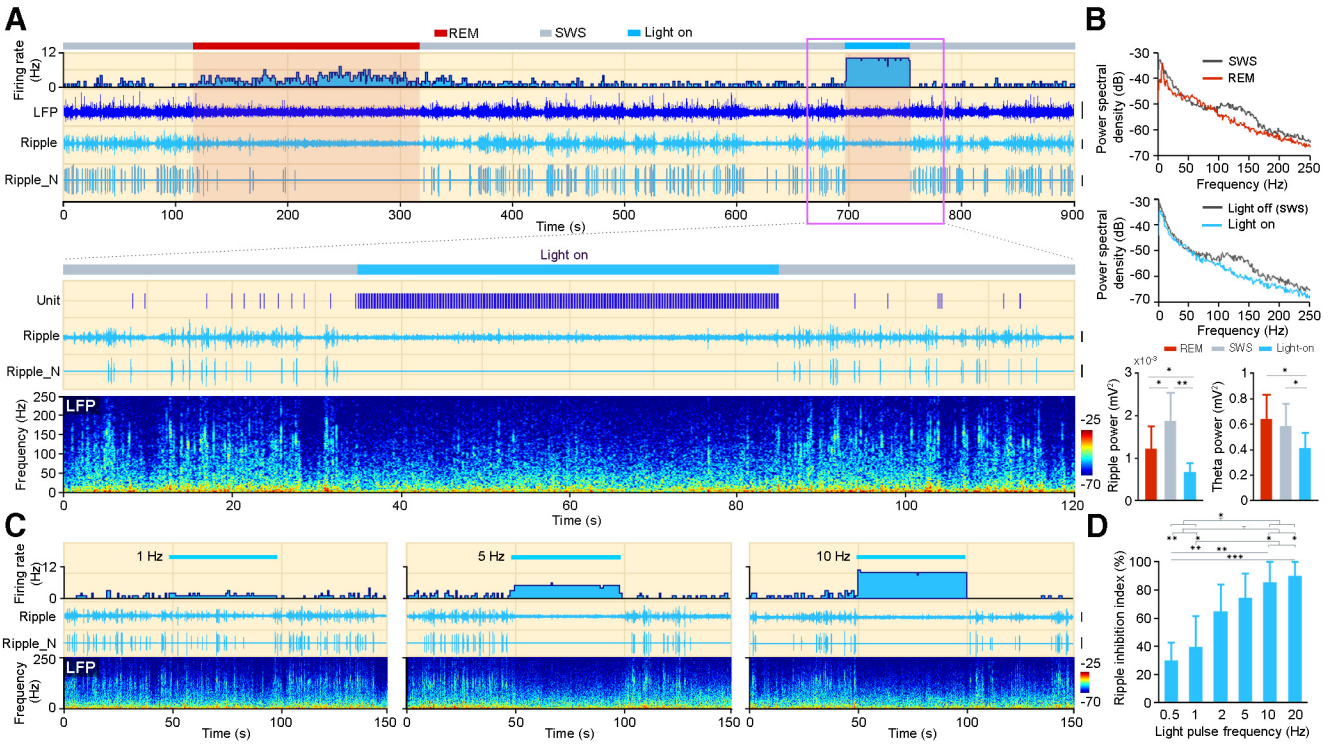

Figure 4. Light-induced MS cholinergic activities suppress CA1 ripple oscillations. ***A***, The 900 s data show the firing activity of one MS ChAT-ChR2 neuron (top, histogram). CA1 LFP, bandpass-filtered ripple, and normalized ripple (Ripple_N) during two different sleep stages (red, REM; gray, SWS) are listed below. The 10 Hz light stimulation was delivered during SWS (blue bar). Note the prolonged increase of neuronal firing and the sustained suppression of ripple oscillations during the persistent light on period. Enlarged view of the pink boxed area is illustrated below with the corresponding LFP power spectrogram at the bottom. Calibration: LFP, 1 mV; Ripple, 0.1 mV; Ripple_N, 0.1 mV. ***B***, Power spectral density of CA1 LFP during SWS, REM, and light-on period. Ripple and theta power of the three stages are calculated and illustrated at the bottom (mean ± SD; for ripple power, $n = 6$ mice; one-way ANOVA, $p = 3.4e\text{-}3$; for theta power, $n = 6$ mice; one-way ANOVA, $p = 0.029$; *post hoc* Holm–Sidak test, $^{*}p < 0.05$, $^{**}p < 0.01$). ***C***, Higher-frequency light-induced firings of the MS cholinergic neuron lead to more suppression of CA1 sharp-wave ripples, similar to ***A***, showing firing rate of a MS ChAT-ChR2 neuron, bandpass-filtered ripple, normalized ripple, and power spectrogram of LFP under different light stimulation frequencies (left, 1 Hz; middle, 5 Hz; right, 10 Hz). Light stimulation was delivered during SWS. Calibration: Ripple, 0.1 mV; Ripple_N, 0.1 mV. ***D***, The suppression of ripple oscillation by different light stimulation frequency (mean ± SD; $n = 7$ mice).

Table 2. Light-induced response on hippocampal theta and gamma oscillations

	AE ($n = 12$)		REM ($n = 9$)	
	Light on	Light off	Light on	Light off
Theta frequency (Hz)	7.43 ± 1.22	7.43 ± 1.17	6.67 ± 0.35	6.24 ± 1
Theta power (mV^2)	0.45 ± 0.21	0.45 ± 0.21	0.58 ± 0.18	0.62 ± 0.25
Gamma power (mV^2)	0.03 ± 0.01	0.03 ± 0.01	0.04 ± 0.03	0.04 ± 0.03

hippocampus (Wess, 1996; Power et al., 2003; Tzavara et al., 2003). We thus injected M_1 to M_4 receptor antagonists into the dorsal CA1 of the hippocampus to determine which subtypes are involved in suppressing hippocampal ripples. After the injection of 39 μg of M_2 receptor antagonist DiM, the ripple event inhibition index dropped from 94 ± 6% to 25 ± 65% (Fig. 6*A*,*B*; $n = 8$ trials from five mice; one-way ANOVA, $p = 2.0e\text{-}4$; *post hoc* Holm–Sidak test: $p = 3.7e\text{-}3$, $t = 3.87$), then rebounded to 96 ± 3% after 2 h. Accordingly, the ripple power inhibition index decreased from 55 ± 13% to 19 ± 36%, and rebounded to 48 ± 16% at the same time scale (Fig. 6*A*,*B*; $n = 8$ trials from five mice; one-way ANOVA, $p = 4.8e\text{-}3$; *post hoc* Holm–Sidak test: $p = 4.4e\text{-}2$, $t = 3.04$). Additional experiments revealed a dose-dependent effect of DiM in rescuing hippocampal ripples (Fig. 6*B*). Similarly, intrahippocampal injection of 8 μg of the muscarinic M_4 receptor antagonist tropicamide resulted in a decrease of ripple event inhibition index from 95 ± 7% to 56 ± 7% (Fig. 6*C*,*D*; $n = 8$ trials from five mice; one-way ANOVA, $p = 9.6e\text{-}3$; *post hoc* Holm–Sidak test: $p = 1.2e\text{-}2$, $t = 3.57$) and a decrease in ripple power inhibition index from 63 ± 14% to 25 ± 12% (Fig. 6*C*,*D*; $n = 8$ trials from five mice; one-way ANOVA: $p = 5.5e\text{-}3$; *post hoc* Holm–Sidak test: $p = 6.3e\text{-}3$, $t = 3.80$) after the injection. Two hours after the injection, cholinergic suppression of hippocampal ripples recovered to the level before injection. In contrast, no significant influence on cholinergic suppression of hippocampal ripples was observed after intrahippocampal microinjection of muscarinic M1 receptor antagonist VU0255035 (after a 5 μg microinjection dose, ripple events inhibition index changed from 98 ± 3% to 98 ± 4%; $n = 8$ trials from two mice for both groups; *t* test: $p = 0.98$, $t = 0.03$) or of M3 receptor antagonist J102149 (after a 38 μg microinjection dose, ripple events inhibition index changed from 97 ± 6% to 93 ± 10%; $n = 8$ trials from three mice for both groups; *t* test: $p = 0.28$, $t = 1.1$).

These results suggest that muscarinic M_2 and M_4 receptors, but not M_1 and M_3 receptors, are involved in the suppression of hippocampal ripples by optogenetic stimulation of MS cholinergic neurons.

Discussion

Combining optogenetics with multichannel *in vivo* recording, we identified and continuously recorded firing activities from MS cholinergic neurons in ChAT-ChR2-EYFP mice for a long period of time (>24 h). We found that MS cholinergic neurons were highly active during exploration, were less active during REM sleep, and were almost inactive during slow-wave sleep. Optogenetic activation of MS cholinergic neurons during SWS

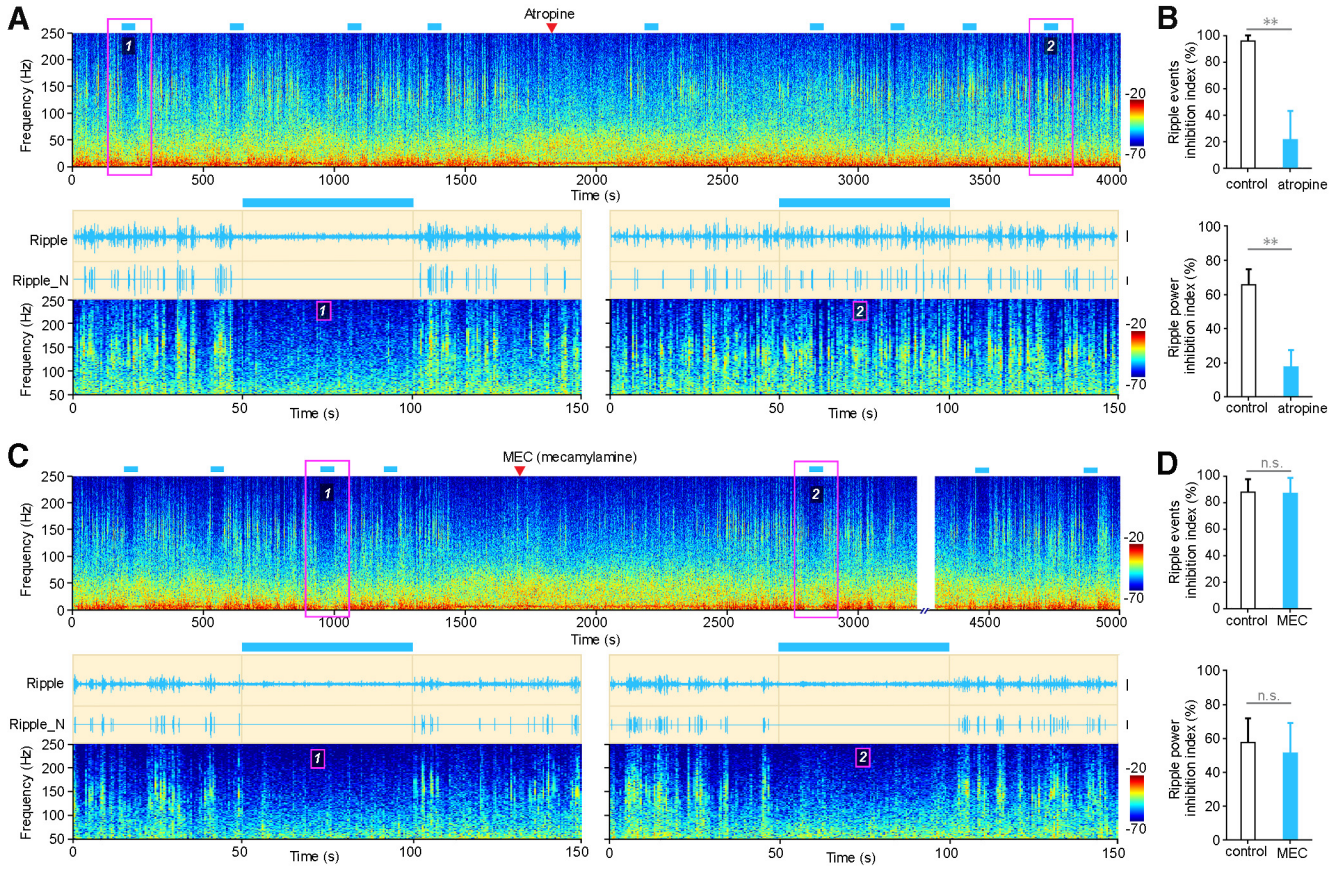

Figure 5. Muscarinic receptors mediate light-induced suppression of ripple oscillations. ***A***, Intraperitoneal injection of atropine successfully rescued light-induced suppression of ripple oscillation. Top, Power spectrogram of 4000 s continuously recorded LFP (red triangle, atropine injection; blue bar, light stimulation). Bottom, Enlarged view of the pink boxed area with additional bandpass-filtered ripple oscillation, showing the rescue effect before (left) and after (right) atropine injection. Calibration: Ripple, 0.2 mV; Ripple_N, 0.2 mV. ***B***, Ripple inhibition is significantly decreased after atropine injection, including ripple incidence (top) and power (bottom) inhibition (mean ± SD; $n = 5$ mice; paired t test, ripple events inhibition index: $^{**}p = 1.7\text{e-}3$, $t = 7.44$; ripple power inhibition index: $^{**}p = 2.0\text{e-}3$, $t = 7.16$). ***C***, ***D***, Same as ***A*** and ***B***, but for intraperitoneal injection of MEC. MEC could not rescue the light-induced suppression of ripple oscillation as there is no significant difference in the reduction of ripple events as well as ripple power before and after MEC injection (*D*; mean ± SD; $n = 6$ mice, paired t test; n.s., not significant; ripple events inhibition index: $p = 0.54$, $t = 0.65$; ripple power inhibition index: $p = 0.22$, $t = 1.41$). Calibration: Ripple, 0.2 mV; Ripple_N, 0.2 mV.

showed a limited effect on hippocampal theta oscillations, but suppression on ripple oscillations. This suppression effect was mediated by mAChRs, but not nAChRs. Furthermore, we identified that muscarinic receptor subtypes M_2 and M_4 were involved in this process.

Previous microdialysis and other studies on the concentration of hippocampal acetylcholine revealed the following brain state-related fluctuations of hippocampal ACh concentration: high ACh concentration during active exploration, lower ACh concentration during REM sleep, and lowest ACh concentration during SWS (Marrosu et al., 1995; Zhang et al., 2010; Teles-Grilo Ruivo et al., 2017). MS cholinergic neurons project directly to the hippocampus and form the major source of acetylcholine to the hippocampus (Lewis et al., 1967; Li et al., 2018). The sleep–wake cycle fluctuation of hippocampal ACh concentration is caused by the firing activity of MS cholinergic neurons, which is consistent with the firing pattern recorded in our experiments. Furthermore, anatomic evidence shows that 93% of the cholinergic axon varicosities in the hippocampus are not associated with junctional specialization, which suggests volume transmission of ACh in these terminals, and only 7% of the cholinergic varicosities form classic synapses and release ACh by wired transmission (Umbriaco et al., 1995; Descarries et al., 1997; Sarter et al., 2009). Correspondingly, the *in vivo* firing patterns of the MS cholinergic neurons that we observed show typical tonic firing patterns, with distinct levels of tonic firing under different brain states. These *in vivo* firing patterns are adapted to the physiological function of regulating hippocampal ACh level under different brain states. In our experiment, we also recorded one slow firing MS cholinergic neuron (firing rates: 0.40 Hz during AE, 0.31 Hz during REM, and 0.05 Hz during SWS). A previous study in head-fixed rats reported medial septal cholinergic cells are slow-firing neurons with an average firing rate of 1.9 Hz in theta state (Simon et al., 2006). Also, an earlier study has reported long-spike septal neurons (putative cholinergic neurons) have a mean firing rate of 28.4 ± 3.0 Hz during animal walking (Brazhnik and Fox, 1997, 1999). These results indicate that MS cholinergic neurons might have heterogeneous firing patterns.

Theta oscillation is prominent in the LFP during AE and REM sleep stages. Thus, these behavior stages are also called theta states (Jouvet, 1969; Vanderwolf, 1969; Buzsáki, 2002). MS cholinergic neurons are highly active during theta states. Despite the temporal coupling of MS cholinergic neuronal activities and hippocampal theta oscillations, optogenetically activating MS cholinergic neurons alone is not sufficient to artificially induce theta oscillations. Instead, it decreased theta power and caused a moderate increase in theta/slow oscillation ratio (theta score) in hippocampal CA1 area (Vandecasteele et al., 2014). However, we did not see such a moderate change in theta score. Relatively low expression of ChR2 on MS cholinergic neurons, limited laser

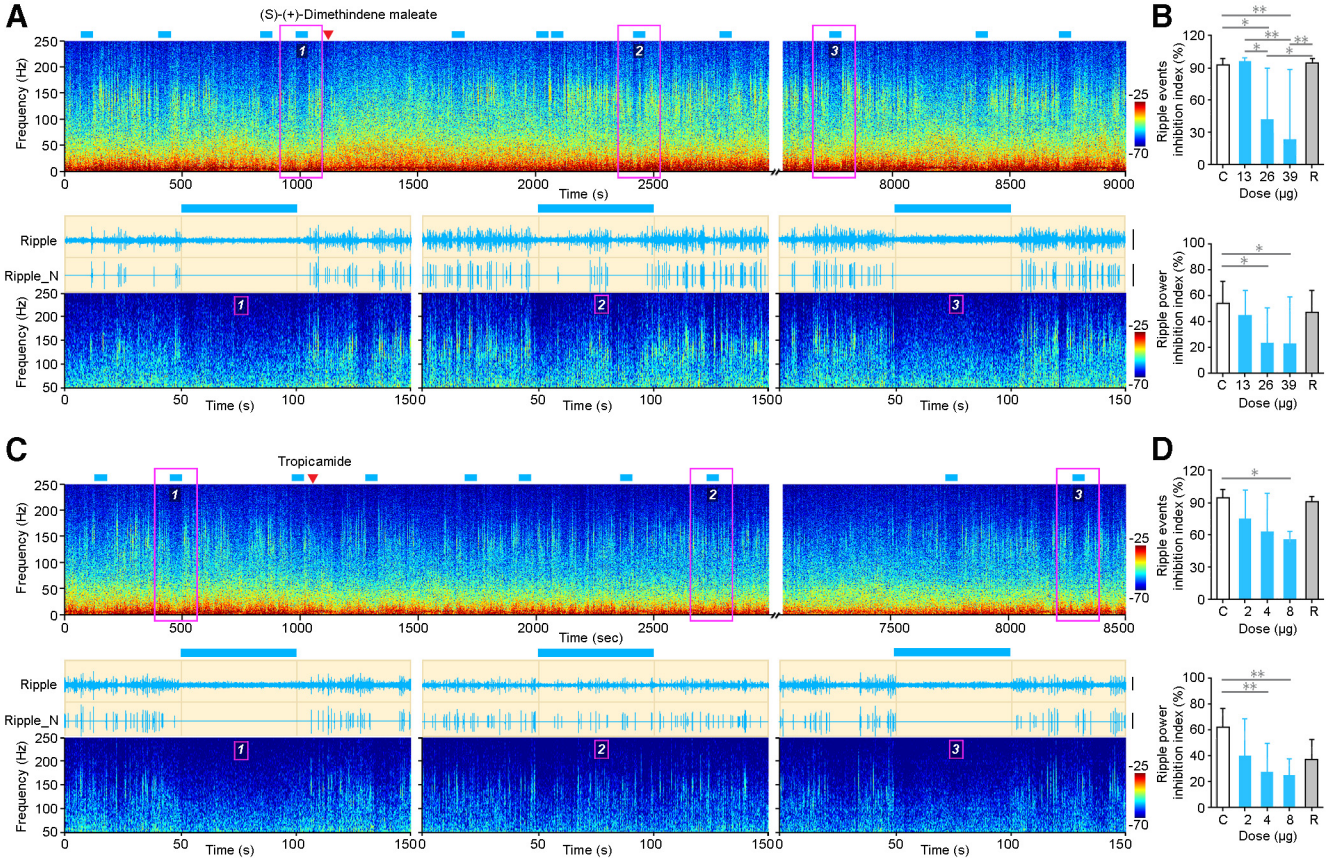

Figure 6. M_2 and M_4 muscarinic receptors mediate light-induced suppression of ripple oscillations. ***A***, Intrahippocampal microinjection of M_2 muscarinic receptor antagonist DiM successfully rescued light-induced suppression of ripple oscillations. Top, Power spectrogram of 9000 s continuously recorded CA1 LFP (red triangle, DiM injection; blue bar, light stimulation). Bottom, Enlarged view of the pink boxed area with additional bandpass-filtered ripple oscillation and normalized ripple signal showing the DiM rescue effect before injection, after injection, and after recovery. Note the recurrence of ripple oscillations during light stimulation in the bottom middle plot. Calibration: Ripple, 0.2 mV; Ripple_N, 0.4 mV. ***B***, Ripple inhibition is significantly decreased after DiM injection, including ripple incidence (top; mean ± SD; one-way ANOVA, $p = 2.0e\text{-}4$; *post hoc* Holm–Sidak test, $^*p < 0.05$, $^{**}p < 0.01$; $n = 8$ trials) and ripple power inhibition index (bottom; mean ± SD; one-way ANOVA, $p = 4.8e\text{-}3$; *post hoc* Holm–Sidak test, $^*p < 0.05$; $n = 8$ trials). Note the dose dependency of DiM on the ripple rescue effect. C, Control; R, recovery. ***C***, ***D***, Same as ***A*** and ***B***, but for intrahippocampal microinjection of M_4 muscarinic receptor antagonist tropicamide. Tropicamide rescued light-induced suppression of ripple oscillation (boxed area 1 of ***C***) as there is ripple incidence after the injection (boxed area 2 of ***C***). Ripple oscillation is reinhibited after the recovery (boxed area 3 of ***C***) from tropicamide injection. Both ripple events and power inhibition index decreased after tropicamide injection (mean ± SD; *post hoc* Holm–Sidak test, $^*p < 0.05$; $^{**}p < 0.01$; control, 2, 4, and 8 μg, $n = 8$ trials; recovery: $n = 4$ trials). Calibration: Ripple, 0.05 mV; Ripple_N, 0.1 mV.

stimulation range could be possible candidate for the decrease of hippocampal theta power on MS cholinergic stimulation. Inhibition of hippocampal ripples by activating MS cholinergic neurons or hippocampal muscarinic receptors has been reported (de Sevilla et al., 2002; Norimoto et al., 2012; Vandecasteele et al., 2014), but the underlying mechanism remains unclear. In this study, we showed that the suppression of hippocampal ripple oscillations by optogenetically activating MS cholinergic neurons during SWS depends on muscarinic acetylcholine receptors, but not nicotinic acetylcholine receptors. Further intrahippocampal injection of various muscarinic receptor antagonists revealed that the cholinergic suppression of ripples acted via muscarinic M_2 and M_4 receptors, and that blocking either type of receptor disrupted the cholinergic suppression of hippocampal ripple oscillations.

High-frequency ripple oscillations in the CA1 region reflect summed IPSPs in ensemble pyramidal neurons as a result of a high-frequency barrage of interneurons. They always co-occur with large depolarizing activities, called sharp waves, forming a sharp wave–ripple complex (Ylinen et al., 1995). Ripples are associated with synchronized firing of CA3 pyramidal neurons. These synchronized activities lead to depolarization of CA1 neurons through Schaffer collaterals, resulting in high-frequency ripple oscillations in the LFP (Buzsáki et al., 1983, 1992; Csicsvari et al., 2000; Sullivan et al., 2011; Fernandez-Ruiz et al., 2012). Immunohistochemistry studies have shown that muscarinic M_4 receptors are located extensively at presynaptic terminals of Schaffer collaterals (Levey et al., 1995; Rouse and Levey, 1996). Activation of M_4 receptors inhibits presynaptic release of glutamate in Schaffer collaterals (Thorn et al., 2017). *In vitro* brain slice recordings also indicate that the activation of CA1 M_4 receptors decreases the amplitude of field EPSPs by 50% under the same Schaffer collateral stimulus (Shirey et al., 2008). Based on these reports, we speculate that, due to the low activity level of MS cholinergic neurons during SWS, the muscarinic M_4 receptors localized at presynaptic terminals of Schaffer collaterals are rarely activated, leading to less inhibition on glutamate release. The absence of inhibition allows synchronous firing of CA3 pyramidal neurons, which leads to large synchronized depolarization in CA1 pyramidal neurons and eventually generates ripples. However, artificially activating MS cholinergic neurons by the optogenetic approach elevates the CA1 ACh concentration to or even goes beyond the physiological ACh level during normal active exploration states. At this point, the

Schaffer collateral M_4 receptors are activated substantially, inhibiting presynaptic release of glutamate and ultimately decreasing the CA1 field EPSP. Despite the firing activities of CA3 pyramidal neurons, large-amplitude synchronized field EPSPs in CA1 are not formed; hence, ripple oscillations are suppressed. Ripples are representative of simultaneous disinhibition of large numbers of pyramidal neurons. This disinhibition is primarily sculpted by interneurons. *In vivo* recording studies reported that firing patterns of some hippocampal interneurons are correlated with high-frequency ripple oscillations (Buzsáki et al., 1992; Klausberger et al., 2003; Wang et al., 2008). Muscarinic M_2 receptors are mainly expressed presynaptically on interneuronal terminals projecting onto the perisomatic region of pyramidal cells (Levey et al., 1995; Rouse and Levey, 1996). Activation of G-protein-coupled G_i metabolic M_2 receptors suppresses GABA transmission (Zhang et al., 2005, 2006). We speculate that high levels of hippocampal ACh induced by optogenetic stimulation during SWS reduce the inhibitory drive to the pyramidal cells generated by ripple-associated interneurons, and eventually suppress ripple oscillations.

The physiological function of the septal–hippocampal cholinergic system has been investigated extensively in recent years. Hippocampal pyramidal neurons respond to transient M_1 mAChR activation with biphasic responses in which inhibition is followed by excitation, whereas prolonged M_1 activation increases neuron excitability (Dasari et al., 2017). Optogenetic activation of septal cholinergic neurons evokes frequency-dependent and behavior state-dependent responses from the noncholinergic septal neurons and hippocampal interneurons (Mamad et al., 2015). In our study, we also recorded single-neuron activities from putative hippocampal pyramidal neurons and interneurons. For both neuron types, they showed increased, decreased, or constant firing rate changes (data not shown). Interestingly, we saw that more pyramidal neurons exhibit suppression of their firing rate compared with those with an increased firing rate. This phenomenon of firing rate was less pronounced in interneurons. This phenomenon by which most pyramidal neurons were suppressed during MS ACh neuron activation was also reported in anesthetized mice (Dannenberg et al., 2015). These results are consistent with the reported suppression of hippocampal ripple oscillations and could also be the underlying mechanism of such inhibition effects.

There are three major types of neurons within the MS, as follows: GABAergic interneurons, cholinergic neurons, and glutamatergic pyramidal neurons. These neurons form a highly interconnected local network within the MS (Borhegyi et al., 2004; Dannenberg et al., 2015; Leão et al., 2015; Robinson et al., 2016). The manipulation of different types of septal neurons shows distinct effects on hippocampal theta oscillations. Activation of MS glutamatergic neurons strongly synchronize hippocampal theta through excitation of local GABAergic and cholinergic neurons within the septum (Robinson et al., 2016). Optogenetic inhibition of MS GABAergic neurons reduces hippocampal theta power and amplitude during REM sleep (Boyce et al., 2016). Furthermore, cholinergic stimulation during SWS completely blocks SWRs, enhances hippocampal theta rhythm, and suppresses peri-theta frequency bands (Vandecasteele et al., 2014). In our study, we used higher-frequency (20 Hz) optic stimulation to intensively activate MS cholinergic neurons during theta states, but failed to see significant changes in CA1 theta oscillations. These results indicated that a high concentration of ACh alone was not sufficient to generate hippocampal theta oscillations in unanesthetized animals. ACh might enhance hippocampal theta by recruiting intraseptal noncholinergic neurons (Dannenberg et al., 2015).

A recent study by Takács et al. (2018) shows some very interesting results. First, they show that the mouse hippocampal cholinergic terminals cotransmit GABA and ACh via different synaptic vesicles. Second, optogenetic activation of MS cholinergic terminals in the hippocampus could suppress spontaneous SWRs with or without ACh antagonists in the *in vitro* hippocampal slice recording. They concluded that the GABAergic component alone can effectively suppress hippocampal SWRs (Takács et al., 2018). But this suppression effect is very weak. There are still a lot of spontaneous SWRs during the light stimulation period. While mice were in the *in vivo* freely moving situation, both the study by Vandecasteele et al. (2014) and our studies have shown that optogenetic activation of MS cholinergic terminals can completely block hippocampal SWRs. We have further shown that hippocampal microinjection of atropine can fully rescue the ripple suppression effect induced by optogenetic activation of MS cholinergic inputs. This result is also different from the *in vitro* slice recording of the study by Takács et al. (2018), where they show no difference with bath application of AChR blockers.

In conclusion, we found theta state-related *in vivo* firing patterns of MS cholinergic neurons by long-period continuous recordings. The activities of these neurons showed temporal coupling with hippocampal theta oscillations. Additionally, our experiments also revealed that one important physiological function of the high activation level of MS cholinergic neurons during theta states, which had not been reported in previous studies, was to suppress hippocampal ripple oscillations by activating muscarinic M_2 and M_4 receptors to ensure theta dominance during this stage.

References

Bader S, Diener M (2015) Novel aspects of cholinergic regulation of colonic ion transport. Pharmacol Res Perspect 3:e00139.

Bland BH (1986) The physiology and pharmacology of hippocampal formation theta rhythms. Prog Neurobiol 26:1–54.

Borhegyi Z, Varga V, Szilágyi N, Fabo D, Freund TF (2004) Phase segregation of medial septal GABAergic neurons during hippocampal theta activity. J Neurosci 24:8470–8479.

Boyce R, Glasgow SD, Williams S, Adamantidis A (2016) Causal evidence for the role of REM sleep theta rhythm in contextual memory consolidation. Science 352:812–816.

Bragin A, Jandó G, Nádasdy Z, Hetke J, Wise K, Buzsáki G (1995) Gamma (40–100 Hz) oscillation in the hippocampus of the behaving rat. J Neurosci 15:47–60.

Brazhnik ES, Fox SE (1997) Intracellular recordings from medial septal neurons during hippocampal theta rhythm. Exp Brain Res 114:442–453.

Brazhnik ES, Fox SE (1999) Action potentials and relations to the theta rhythm of medial septal neurons in vivo. Exp Brain Res 127:244–258.

Buzsáki G (1986) Hippocampal sharp waves: their origin and significance. Brain Res 398:242–252.

Buzsáki G (2002) Theta oscillations in the hippocampus. Neuron 33:325–340.

Buzsáki G, Leung LW, Vanderwolf CH (1983) Cellular bases of hippocampal EEG in the behaving rat. Brain Res 6:139–171.

Buzsáki G, Horvath Z, Urioste R, Hetke J, Wise K (1992) High-frequency network oscillation in the hippocampus. Science 256:1025–1027.

Carr MF, Jadhav SP, Frank LM (2011) Hippocampal replay in the awake state: a potential substrate for memory consolidation and retrieval. Nat Neurosci 14:147–153.

Csicsvari J, Hirase H, Czurkó A, Mamiya A, Buzsáki G (1999) Oscillatory coupling of hippocampal pyramidal cells and interneurons in the behaving rat. J Neurosci 19:274–287.

Csicsvari J, Hirase H, Mamiya A, Buzsáki G (2000) Ensemble patterns of hippocampal CA3-CA1 neurons during sharp wave-associated population events. Neuron 28:585–594.

Csicsvari J, Jamieson B, Wise KD, Buzsáki G (2003) Mechanisms of gamma oscillations in the hippocampus of the behaving rat. Neuron 37:311–322.

Czurkó A, Huxter J, Li Y, Hangya B, Muller RU (2011) Theta phase classification of interneurons in the hippocampal formation of freely moving rats. J Neurosci 31:2938–2947.

Dannenberg H, Pabst M, Braganza O, Schoch S, Niediek J, Bayraktar M, Mormann F, Beck H (2015) Synergy of direct and indirect cholinergic septo-hippocampal pathways coordinates firing in hippocampal networks. J Neurosci 35:8394–8410.

Dasari S, Hill C, Gulledge AT (2017) A unifying hypothesis for M1 muscarinic receptor signalling in pyramidal neurons. J Physiol 595:1711–1723.

Descarries L, Gisiger V, Steriade M (1997) Diffuse transmission by acetylcholine in the CNS. Prog Neurobiol 53:603–625.

de Sevilla DF, Cabezas C, de Prada ANO, Sánchez-Jiménez A, Buño W (2002) Selective muscarinic regulation of functional glutamatergic Schaffer collateral synapses in rat CA1 pyramidal neurons. J Physiol 545:51–63.

Fernandez-Ruiz A, Makarov VA, Benito N, Herreras O (2012) Schaffer-specific local field potentials reflect discrete excitatory events at gamma frequency that may fire postsynaptic hippocampal CA1 units. J Neurosci 32:5165–5176.

Girardeau G, Benchenane K, Wiener SI, Buzsáki G, Zugaro MB (2009) Selective suppression of hippocampal ripples impairs spatial memory. Nat Neurosci 12:1222–1223.

Grastyán E, Lissák K, Madarász I, Donhoffer H (1959) Hippocampal electrical activity during the development of conditioned reflexes. Electroencephalogr Clin Neurophysiol 11:409–430.

Grossman N, Nikolic K, Grubb MS, Burrone J, Toumazou C, Degenaar P (2011) High-frequency limit of neural stimulation with ChR2. Conference proceedings: Annual International Conference of the IEEE Engineering in Medicine and Biology Society IEEE Engineering in Medicine and Biology Society Annual Conference 2011:4167–4170

Hajszan T, Alreja M, Leranth C (2004) Intrinsic vesicular glutamate transporter 2-immunoreactive input to septohippocampal parvalbumin-containing neurons: novel glutamatergic local circuit cells. Hippocampus 14:499–509.

Hernández M, Simonsen U, Prieto D, Rivera L, García P, Ordaz E, García-Sacristán A (1993) Different muscarinic receptor subtypes mediating the phasic activity and basal tone of pig isolated intravesical ureter. Br J Pharmacol 110:1413–1420.

Honda K, Ando S, Koga K, Takano Y (2004) The spinal muscarinic receptor subtypes contribute to the morphine-induced antinociceptive effects in thermal stimulation in mice. Neurosci Lett 371:235–238.

Jouvet M (1969) Biogenic amines and the states of sleep. Science 163:32–41.

Kiss J, Patel AJ, Baimbridge KG, Freund TF (1990) Topographical localization of neurons containing parvalbumin and choline acetyltransferase in the medial septum-diagonal band region of the rat. Neuroscience 36:61–72.

Klausberger T, Magill PJ, Márton LF, Roberts JD, Cobden PM, Buzsáki G, Somogyi P (2003) Brain-state- and cell-type-specific firing of hippocampal interneurons in vivo. Nature 421:844–848.

Kurowski P, Gawlak M, Szulczyk P (2015) Muscarinic receptor control of pyramidal neuron membrane potential in the medial prefrontal cortex (mPFC) in rats. Neuroscience 303:474–488.

Lambrecht G, Gross J, Mutschler E (1999) Neuronal soma-dendritic and prejunctional M1-M4 receptors in gastrointestinal and genitourinary smooth muscle. Life Sci 64:403–410.

Lazareno S, Buckley NJ, Roberts FF (1990) Characterization of muscarinic M4 binding sites in rabbit lung, chicken heart, and NG108-15 cells. Mol Pharmacol 38:805–815.

Leão RN, Targino ZH, Colom LV, Fisahn A (2015) Interconnection and synchronization of neuronal populations in the mouse medial septum/diagonal band of Broca. J Neurophysiol 113:971–980.

Levey AI, Edmunds SM, Koliatsos V, Wiley RG, Heilman CJ (1995) Expression of m1-m4 muscarinic acetylcholine receptor proteins in rat hippocampus and regulation by cholinergic innervation. J Neurosci 15:4077–4092.

Lewis PR, Shute CC, Silver A (1967) Confirmation from choline acetylase analyses of a massive cholinergic innervation to the rat hippocampus. J Physiol 191:215–224.

Li X, Yu B, Sun Q, Zhang Y, Ren M, Zhang X, Li A, Yuan J, Madisen L, Luo Q, Zeng H, Gong H, Qiu Z (2018) Generation of a whole-brain atlas for the cholinergic system and mesoscopic projectome analysis of basal forebrain cholinergic neurons. Proc Natl Acad Sci U S A 115:415–420.

Lin L, Chen G, Xie K, Zaia KA, Zhang S, Tsien JZ (2006) Large-scale neural ensemble recording in the brains of freely behaving mice. J Neurosci Methods 155:28–38.

Mamad O, McNamara HM, Reilly RB, Tsanov M (2015) Medial septum regulates the hippocampal spatial representation. Front Behav Neurosci 9:166.

Marrosu F, Portas C, Mascia MS, Casu MA, Fa M, Giagheddu M, Imperato A, Gessa GL (1995) Microdialysis measurement of cortical and hippocampal acetylcholine release during sleep-wake cycle in freely moving cats. Brain Res 671:329–332.

Melonakos ED, White JA, Fernandez FR (2019) A model of cholinergic suppression of hippocampal ripples through disruption of balanced excitation/inhibition. Hippocampus 29:773–786.

Miller SL, Aroniadou-Anderjaska V, Pidoplichko VI, Figueiredo TH, Apland JP, Krishnan JK, Braga MF (2017) The M_1 muscarinic receptor antagonist VU0255035 delays the development of status epilepticus after organophosphate exposure and prevents hyperexcitability in the basolateral amygdala. J Pharmacol Exp Ther 360:23–32.

Mizumori SJ, Perez GM, Alvarado MC, Barnes CA, McNaughton BL (1990) Reversible inactivation of the medial septum differentially affects two forms of learning in rats. Brain Res 528:12–20.

Norimoto H, Mizunuma M, Ishikawa D, Matsuki N, Ikegaya Y (2012) Muscarinic receptor activation disrupts hippocampal sharp wave-ripples. Brain Res 1461:1–9.

Pfaff O, Hildebrandt C, Waelbroeck M, Hou X, Moser U, Mutschler E, Lambrecht G (1995) The (S)-(+)-enantiomer of dimethindene: a novel M2-selective muscarinic receptor antagonist. Eur J Pharmacol 286:229–240.

Pfeiffer BE, Foster DJ (2013) Hippocampal place-cell sequences depict future paths to remembered goals. Nature 497:74–79.

Power AE, Vazdarjanova A, McGaugh JL (2003) Muscarinic cholinergic influences in memory consolidation. Neurobiol Learn Mem 80:178–193.

Prince J, Lundgren A, Stadnisky MD, Nash WT, Beeber A, Turner SD, Brown MG (2013) Multiparametric analysis of host response to murine cytomegalovirus in MHC class I-disparate mice reveals primacy of D^k-licensed $Ly49G_2^+$ NK cells in viral control. J Immunol 191:4709–4719.

Rawlins JN, Feldon J, Gray JA (1979) Septo-hippocampal connections and the hippocampal theta rhythm. Exp Brain Res 37:49–63.

Robinson J, Manseau F, Ducharme G, Amilhon B, Vigneault E, El Mestikawy S, Williams S (2016) Optogenetic activation of septal glutamatergic neurons drive hippocampal theta rhythms. J Neurosci 36:3016–3023.

Rouse ST, Levey AI (1996) Expression of m1-m4 muscarinic acetylcholine receptor immunoreactivity in septohippocampal neurons and other identified hippocampal afferents. J Comp Neurol 375:406–416.

Sarter M, Parikh V, Howe WM (2009) Phasic acetylcholine release and the volume transmission hypothesis: time to move on. Nat Rev Neurosci 10:383–390.

Seki Y, Tomyta K (2019) Effects of metronomic sounds on a self-paced tapping task in budgerigars and humans. Curr Zool 65:121–128.

Sheffler DJ, Williams R, Bridges TM, Xiang Z, Kane AS, Byun NE, Jadhav S, Mock MM, Zheng F, Lewis LM, Jones CK, Niswender CM, Weaver CD, Lindsley CW, Conn PJ (2009) A novel selective muscarinic acetylcholine receptor subtype 1 antagonist reduces seizures without impairing hippocampus-dependent learning. Mol Pharmacol 76:356–368.

Shen X, Voets NL, Larkin SJ, de Pennington N, Plaha P, Stacey R, McCullagh JSO, Schofield CJ, Clare S, Jezzard P, Cadoux-Hudson T, Ansorge O, Emir UE (2019) A noninvasive comparison study between human gliomas with IDH1 and IDH2 mutations by MR spectroscopy. Metabolites 9:35.

Shirey JK, Xiang Z, Orton D, Brady AE, Johnson KA, Williams R, Ayala JE, Rodriguez AL, Wess J, Weaver D, Niswender CM, Conn PJ (2008) An allosteric potentiator of M4 mAChR modulates hippocampal synaptic transmission. Nat Chem Biol 4:42–50.

Siapas AG, Lubenov EV, Wilson MA (2005) Prefrontal phase locking to hippocampal theta oscillations. Neuron 46:141–151.

Simon AP, Poindessous-Jazat F, Dutar P, Epelbaum J, Bassant MH (2006) Firing properties of anatomically identified neurons in the medial septum of anesthetized and unanesthetized restrained rats. J Neurosci 26:9038–9046.

Sotty F, Danik M, Manseau F, Laplante F, Quirion R, Williams S (2003) Distinct electrophysiological properties of glutamatergic, cholinergic and GABAergic rat septohippocampal neurons: novel implications for hippocampal rhythmicity. J Physiol 551:927–943.

Sullivan D, Csicsvari J, Mizuseki K, Montgomery S, Diba K, Buzsáki G (2011) Relationships between hippocampal sharp waves, ripples, and fast gamma oscillation: influence of dentate and entorhinal cortical activity. J Neurosci 31:8605–8616.

Sun Y, Nguyen AQ, Nguyen JP, Le L, Saur D, Choi J, Callaway EM, Xu X (2014) Cell-type-specific circuit connectivity of hippocampal CA1 revealed through Cre-dependent rabies tracing. Cell Rep 7:269–280.

Takács VT, Cserép C, Schlingloff D, Pósfai B, Szőnyi A, Sos KE, Környei Z, Dénes Á, Gulyás AI, Freund TF, Nyiri G (2018) Co-transmission of acetylcholine and GABA regulates hippocampal states. Nat Commun 9:2848.

Teles-Grilo Ruivo LM, Baker KL, Conway MW, Kinsley PJ, Gilmour G, Phillips KG, Isaac JTR, Lowry JP, Mellor JR (2017) Coordinated acetylcholine release in prefrontal cortex and hippocampus is associated with arousal and reward on distinct timescales. Cell Rep 18:905–917.

Thorn CA, Popiolek M, Stark E, Edgerton JR (2017) Effects of M1 and M4 activation on excitatory synaptic transmission in CA1. Hippocampus 27:794–810.

Tsentsevitsky AN, Kovyazina IV, Nurullin LF, Nikolsky EE (2017) Muscarinic cholinoreceptors (M1-, M2-, M3- and M4-type) modulate the acetylcholine secretion in the frog neuromuscular junction. Neurosci Lett 649:62–69.

Tzavara ET, Bymaster FP, Felder CC, Wade M, Gomeza J, Wess J, McKinzie DL, Nomikos GG (2003) Dysregulated hippocampal acetylcholine neurotransmission and impaired cognition in M2, M4 and M2/M4 muscarinic receptor knockout mice. Mol Psychiatry 8:673–679.

Umbriaco D, Garcia S, Beaulieu C, Descarries L (1995) Relational features of acetylcholine, noradrenaline, serotonin and GABA axon terminals in the stratum radiatum of adult rat hippocampus (CA1). Hippocampus 5:605–620.

Vandecasteele M, Varga V, Berényi A, Papp E, Barthó P, Venance L, Freund TF, Buzsáki G (2014) Optogenetic activation of septal cholinergic neurons suppresses sharp wave ripples and enhances theta oscillations in the hippocampus. Proceedings of the National Academy of Sciences 111:13535–13540.

Vanderwolf CH (1969) Hippocampal electrical activity and voluntary movement in the rat. Electroencephalogr Clin Neurophysiol 26:407–418.

Veeraragavan S, Bui N, Perkins JR, Yuva-Paylor LA, Paylor R (2011) The modulation of fragile X behaviors by the muscarinic M4 antagonist, tropicamide. Behav Neurosci 125:783–790.

Wang Y, Zhang L, Pan J, Xie K, Li S, Wang Z, Lin L (2008) Ripple-associated high-firing interneurons in the hippocampal CA1 region. Sci China Ser C Life Sci 51:120–126.

Wess J (1996) Molecular biology of muscarinic acetylcholine receptors. Crit Rev Neurobiol 10:69–99.

Yang Y, Liu B, Xu J, Wang J, Wu J, Shi C, Xu Y, Dong J, Wang C, Lai W, Zhu J, Xiong L, Zhu D, Li X, Yang W, Yamauchi T, Sugawara A, Li Z, Sun F, Li X, et al. (2017) Derivation of pluripotent stem cells with in vivo embryonic and extraembryonic potency. Cell 169:243–257.

Ylinen A, Bragin A, Nadasdy Z, Jando G, Szabo I, Sik A, Buzsáki G (1995) Sharp wave-associated high-frequency oscillation (200 Hz) in the intact hippocampus: network and intracellular mechanisms. J Neurosci 15:30–46.

Zhang H, Lin SC, Nicolelis MA (2010) Spatiotemporal coupling between hippocampal acetylcholine release and theta oscillations *in vivo*. J Neurosci 30:13431–13440.

Zhang HM, Li DP, Chen SR, Pan HL (2005) M_2, M_3, and M_4 receptor subtypes contribute to muscarinic potentiation of GABAergic inputs to spinal dorsal horn neurons. J Pharmacol Exp Ther 313:697–704.

Zhang HM, Chen SR, Matsui M, Gautam D, Wess J, Pan HL (2006) Opposing functions of spinal M_2, M_3, and M_4 receptor subtypes in regulation of GABAergic inputs to dorsal horn neurons revealed by muscarinic receptor knockout mice. Mol Pharmacol 69:1048–1055.

Zhao S, Ting JT, Atallah HE, Qiu L, Tan J, Gloss B, Augustine GJ, Deisseroth K, Luo M, Graybiel AM, Feng G (2011) Cell type-specific channelrhodopsin-2 transgenic mice for optogenetic dissection of neural circuitry function. Nat Methods 8:745–752.